Preprint
UCRL-JC-134916

High-Resolution Measurements of the K-Shell Spectral Lines of Hydrogenlike and Heliumlike Xenon

K. Widmann, P. Beiersdorfer, G.V. Brown, J.R. Crespo Lopez-Urrutia, A.L. Osterheld, K.J. Reed, J.H. Scofield, S.B. Utter

This article was submitted to
18th International Conference on X-Ray and Inner-Shell Processes,
Chicago, IL, August 23-27, 1999

September 13, 1999

U.S. Department of Energy
Lawrence Livermore National Laboratory

High–Resolution Measurements of the K–Shell Spectral Lines of Hydrogenlike and Heliumlike Xenon

Klaus Widmann[1], Peter Beiersdorfer, Gregory V. Brown, José R. Crespo López–Urrutia[2], Albert L. Osterheld, Kennedy J. Reed, James H. Scofield, and Steven B. Utter

Department of Physics, Lawrence Livermore National Laboratory, P.O.Box 808, Livermore, CA, 94551, USA

Abstract. With the implementation of a transmission–type curved crystal spectrometer at the Livermore high–energy electron beam ion trap (SuperEBIT) the window on sub–eV level measurements of the ground–state quantum electrodynamics and the two–electron quantum electrodynamics of high–Z ions has been opened. High–resolution spectroscopic measurements of the Kα spectra of hydrogenlike Xe^{53+} and heliumlike Xe^{52+} are presented. The electron–impact excitation cross sections have been determined relative to the radiative recombination cross sections. The electron–impact energy was 112 keV which is about 3.7 times the excitation threshold for the $n = 2 \rightarrow 1$ transitions. Although the relative uncertainties of the measured electron–impact excitation cross sections range from about 20% to 50% , significant disagreement between the measured and calculated cross section values has been found for one of the heliumlike xenon lines. Overall, the comparison between experiment and theory shows that already for xenon (Z=54) the Breit interaction plays a significant part in the collisional excitation process. The measured cross sections for the hydrogenlike transitions are in good agreement with theoretical predictions. Additionally, the Xe^{53+} Ly–α_1 transition energy has been measured utilizing the Kα emission of neutral cesium and barium for calibration. Surprisingly, the experimental result, (31279.2 $\pm$ 1.5) eV, disagrees with the widely accepted theoretically predicted value of (31283.77 $\pm$ 0.09) eV. However, this disagreement does not (yet) call for any correction in respect to the theoretical values for the transition energies of the hydrogenlike isoelectronic sequence. It rather emphasizes the need for a re–evaluation of the commonly used x–ray wavelengths table for atomic inner–shell transitions, in particular, for the cesium Kα lines.

---

1) E–mail: widmann1@llnl.gov.
2) Present address: Fakultät für Physik, Albert–Ludwigs–Universität Freiburg, D–79104 Freiburg, Germany

INTRODUCTION

High–resolution spectroscopic measurements of the K–shell spectra of highly charged heavy ions are the key to sub–eV level measurements of the ground–state quantum electrodynamics (QED) and the two–electron QED, respectively [1]. In particular, precise measurements of the 1s–Lambshift of hydrogenlike ions are being persued by several research groups around the world [2]. The most precise tests of QED for highly charged heavy ions, however, are utilizing intra L–shell transitions of lithiumlike ions, such as U^{89+}, Th^{87+}, and Bi^{80+} [3–6], where high–resolution crystal spectrometers can be employed. The experimental precision of these QED–test measurements is in the 0.1% regime [6].

The increased "visibility" of QED and relativistic effects in high–Z few–electron systems[3] is, unfortunately, also accompanied by an increased impact of the nuclear properties on the atomic structure [7]. Utilization of high–resolution spectrometers is essential. In particular, the acquisition of well resolved spectral features is necessary for the experimental determination of electron–ion collision cross sections, e.g., the electron–impact excitation cross sections, which play an important role for an accurate interpretation and, hence, for reliable predictions of the atomic processes that take place in the x–ray emitting sources. In contrast to the energy–level studies, there is only a small pool of experimental cross–section values available for highly charged ions, especially, for the electron–impact excitation [8,9], which is certainly a drawback for the development of accurate electron–ion collision models. The qualitative and quantitative analysis of the spectral information obtained from the emission of high–Z ions in very high–temperature plasmas depends on these models. Thus, an experimentally well–supported atomic database is needed [10].

High–resolution spectroscopic investigations of the K–shell emission of highly charged ions have been performed for x–ray energies up to 13 keV, i.e, the $n = 2 \rightarrow 1$ transitions in heliumlike Kr^{34+} [11–13]. The implementation of a transmission–type curved crystal spectrometer at the Livermore high–energy electron beam ion trap (SuperEBIT) enables to push these high–resolution measurements into the hard x–ray regime. The observation of hydrogenlike and heliumlike xenon spectra prove the feasibility of this transmission–type crystal spectrometer. The fine–structure–resolved spectrum of the $K\alpha$ emission of the Xe^{53+} and Xe^{52+} ions gives access to transition–energy and relative line–intensity measurements. From the charge–specific determination of the line intensities the electron–impact excitation cross sections are inferred relative to the cross sections for the radiative recombination lines. Xenon was the element of choice due to its potential use in the next–generation fusion devices, such as the National Ignition Facility (NIF) or the International Thermonuclear Experimental Reactor (ITER), which are proposed

---

[3] The approximate scaling behavior for both, relativistic and QED effects, is Z^4.

to have electron temperatures in excess of 30 keV. In such a high–temperature plasma only heavy elements like xenon would still have a significant abundance in the heliumlike charge state (Xe^{52+}), which is the preferred charge state for plasma diagnostics based on x–ray spectroscopy. Low–Z and mid–Z elements would be completely ionized under these conditions. Another advantage of admixing a high–Z element to the fusion plasma is the strong scaling of radiative transitions and, thus, radiative cooling power with Z. The technological challenge of admixing and removing the high–Z trace element to and from the plasma chamber favors the use of a noble gas, e.g., xenon.

This paper is organized as follows. The first section, "**SuperEBIT operation**", gives a brief description about the SuperEBIT operating parameters that have been used for the production and trapping of the highly charged xenon ions. Section two, "**Transmission–type curved crystal spectrometer**", describes the design and performance of the transmission–type curved crystal spectrometer that has been used for the high–resolution measurements of the Kα emission of hydrogenlike and heliumlike xenon. The spectra are presented in the third section, "**Kα spectra of Xe^{53+} and Xe^{52+}**". The contribution of the various radiative and collisional atomic processes present in the SuperEBIT trap region to the measured relative line intensities is discussed in section four, "**Determination of the electron–impact excitation cross sections**". Section five, "**Measurement of the transition energies**", is dedicated to the measurement of the Ly–α_1 transition energy of hydrogenlike xenon utilizing the Kα emission of neutral cesium and barium for calibration. A summary and discussion of the results is presented in the sixth and final section, "**Discussion**".

SUPEREBIT OPERATION

The Livermore SuperEBIT facility is capable of producing, trapping, and exciting any kind of highly charged ions [14,15] up to bare uranium (U^{92+}) [16]. The cylindrical trap region measures about 2 cm in axial direction, i.e., along the electron beam. In radial direction, the confinement for the ions is given by the space charge of the electron beam, which is compressed by a 3–Tesla strong magnetic field to a diameter of about 100 μm [17].

The x–ray emission can be observed perpendicular to the electron beam through round apertures of 1.27 cm diameter. For the investigation of the highly charged xenon x–ray emission, neutral xenon atoms are injected into SuperEBIT by means of a pulsed gas injection system. A continuous flow of neon was also introduced into the trap region in order to supply light ions for the evaporative cooling process [18,19]. The gas injector pressure for the neon cooling was on the order of $2.6 \cdot 10^{-8}$ Torr ($\approx 3.5 \cdot 10^{-6}$ Pa). The xenon injection pressure was above $6 \cdot 10^{-8}$ Torr ($\approx 8 \cdot 10^{-6}$ Pa) during the injection pulse.

The electron beam energy was set to 112 keV in order to obtain a charge balance

that is dominated by the heliumlike and hydrogenlike species[4], and the electron beam current was 250 mA. The duration of a "timing" or "trapping" cycle was 11.2 s. One cycle includes injection of xenon gas, ionization until the high charge states are obtained, a period of data acquisition, and dumping of the ions before other high–Z elements intrinsic to the SuperEBIT device, such as barium and tungsten from the electron gun assembly, accumulate in the trap.

A high–purity germanium detector is used to record the x–ray radiation emitted from the trap region. These broadband spectra — as shown in Figure 1a — include the directly excited lines $K\alpha, \beta, \gamma, \ldots$ around 30 keV, the continuous Bremsstrahlung below the electron beam energy, and the radiative recombination lines. The line character of these free–to–bound transitions is due to the narrow energy–band width of the electron beam. The radiative recombination lines are labeled according to the atomic shell into which the electron was captured. The radiative recombination spectrum gives access to the charge distribution in the trap region. Using calculated values for the ionization energy and the radiative recombination cross sections for each charge state [20], a fit of the spectral features (see Figure 1b) yields the relative abundance of the highly charged xenon ions. An absolute number density of the ions can be derived by taking into account the solid angle, the detector efficiency, and the attenuation of the x–rays along their path from the trap region to the detector. The result of this charge state distribution measurement is listed in Table 1.

TABLE 1. Fractional and absolute ion abundances (f_n, N) of trapped highly charged xenon ions ($Xe^{54+\ldots51+}$). The abundances were determined using the line intensities of the radiative recombination transitions onto the K–shell and L–shell (see Figure 1). The ion density values (n) are based on a cylindrical trap geometry of 1.27 cm in height and 0.01 cm in diameter.

Ion species	f_N	N	n cm^{-3}
bare Xe^{54+}	0.051 ± 0.003	9200 ± 1300	(0.86 ± 0.12) $\cdot 10^8$
H–like Xe^{53+}	0.184 ± 0.010	33200 ± 4800	(3.10 ± 0.44) $\cdot 10^8$
He–like Xe^{52+}	0.631 ± 0.033	117000 ± 19000	(11.0 ± 1.8) $\cdot 10^8$
Li–like Xe^{51+}	0.139 ± 0.043	20800 ± 7100	(1.94 ± 0.66) $\cdot 10^8$

TRANSMISSION–TYPE CURVED CRYSTAL SPECTROMETER

Besides the reduced crystal reflectivity at small Bragg angles, crystal spectrometers that depend on spatially resolved detection of the diffracted x rays also suffer from the tremendous decrease in efficiency of the position sensitive detectors at

[4] Heliumlike and hydrogenlike xenon have ionization potentials of $E_{He\rightarrow H} = 40.3$ keV and $E_{H\rightarrow bare} = 41.3$ keV, respectively.

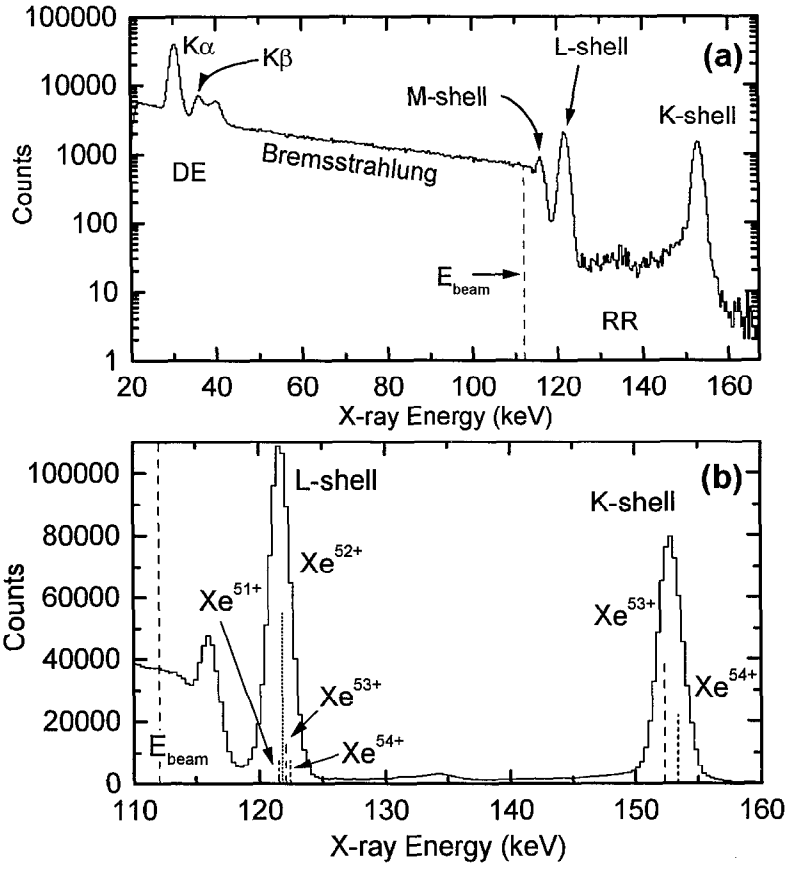

FIGURE 1. Direct excitation (DE) and radiative recombination (RR) spectra of highly charged xenon ions measured with a germanium detector. Spectrum **(a)** which was taken during an one–hour measuring period shows the ratio between the DE and RR emission. The dashed and dotted lines in the RR spectrum displayed in **(b)** — acquired over several days — mark the positions of the RR lines obtained by adding the ionization energy that is being released upon recombination to the beam energy, which was set to 112.1 keV.

higher x–ray energies [21]. Thus, for the hard x–ray regime, a transmission–type curved crystal spectrometer was developed based on the DuMond design [22]. The choice of a transmission–type spectrometer was favoured by the larger solid angle achievable with the same crystal geometry due to the perpendicular orientation of the lattice planes with respect to the crystal surface. The DuMond geometry, which employs a cylindrically bent crystal, requires that the radius of curvature of the crystal is the diameter of the so–called Rowland circle and that the center of the source (or spectrometer entrance slit) and the center of the crystal are part of this circle as shown in Figure 2. A crystal that is curved in such a way offers the incoming x rays a much larger area with the same Bragg angle in comparison with a flat crystal. Thus, the curved design increases the spectral throughput, i.e., the transmitted flux per energy interval, tremendously. Correct curvature and

placement also strongly reduce the overall bandwidth of the diffracted x rays. The goal of the SuperEBIT transmission–type spectrometer design was to reduce this bandwidth such that the spectrometer can be used as a monochromator, where no spatially resolved detection of the diffracted x rays is necessary, and detectors with almost 100% counting efficiency can be used, like high–purity germanium detectors. The energy dispersion of the germanium detector in such an arrangement serves as a tool for the suppression of the background radiation.

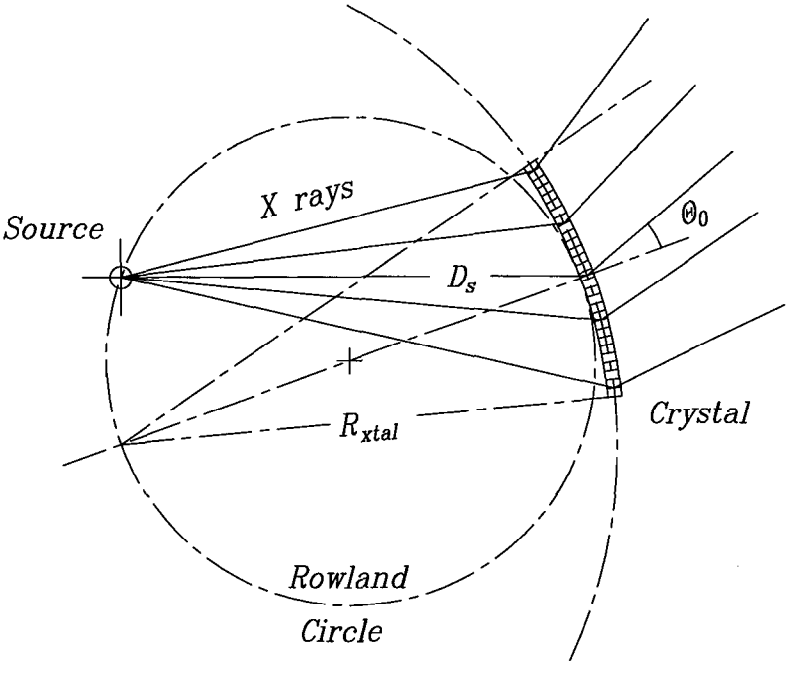

FIGURE 2. Geometric requirements of the DuMond–type crystal spectrometer. The curvature of the cylindrically bent crystal R_{xtal} equals the diameter of the Rowland circle. Placing the center of the source and the center of the crystal on the Rowland circle defines the distance between these points as a function of the central Bragg angle θ_0, i.e., $D_s = R_{xtal} \cos\theta_0$.

For the following measurements, the spectrometer utilizes a $(140 \times 40 \times 0.6)$ mm^3 quartz crystal with a $(13\bar{4}0)$ orientation. The 2d spacing of this crystal is 2.3604 Å [23] and, thus, the Bragg angle for the diffraction of the 30–keV x rays is around 10°. The radius of curvature of the crystal was $\approx$ 2.5 m. The crystal is rotated by means of a high–precision stepper motor which is mounted on a modified rotation stage. The stepper motor has a unidirectional repeatability of $\pm 1\,\mu$m, and the uncertainty with respect to the traveled range is $\pm 5\,\mu$m. In combination with the $6\frac{3}{8}$" (≈ 161.9 mm) lever of the modified rotation stage, minimum angular increments of 0.00035° are achievable. To take advantage of this high unidirectional precision, all scans were performed by always rotating the crystal in the same manner, e.g., counter–clockwise.

The spectrometer performance was tested using a 1–mCi ^{133}Ba source and a 75–μm wide and 12.7–mm tall slit made out of 2.4–mm thick tantalum. The radioiso-

tope ^{133}Ba decays by capturing an innershell electron, thus, creating an innershell excited cesium atom. The characteristic K–shell x rays of cesium are centered around 31.0 keV ($K\alpha_1$) and 30.6 keV ($K\alpha_2$). The spectrum was obtained by rotating the crystal in small increments and counting the number of diffracted x rays for a certain time before rotating the crystal to the next position. Figure 3 shows the result of several scans over both lines. The measured line width of 30 eV contains the instrumental width and also the natural line width of the cesium $K\alpha$ radiation, which is about 15 eV for $K\alpha_1$ [24]. Deconvolution of the measured profile leads to an instrumental line width of about 25 eV, which is equivalent to a resolving power of ≈ 1200.

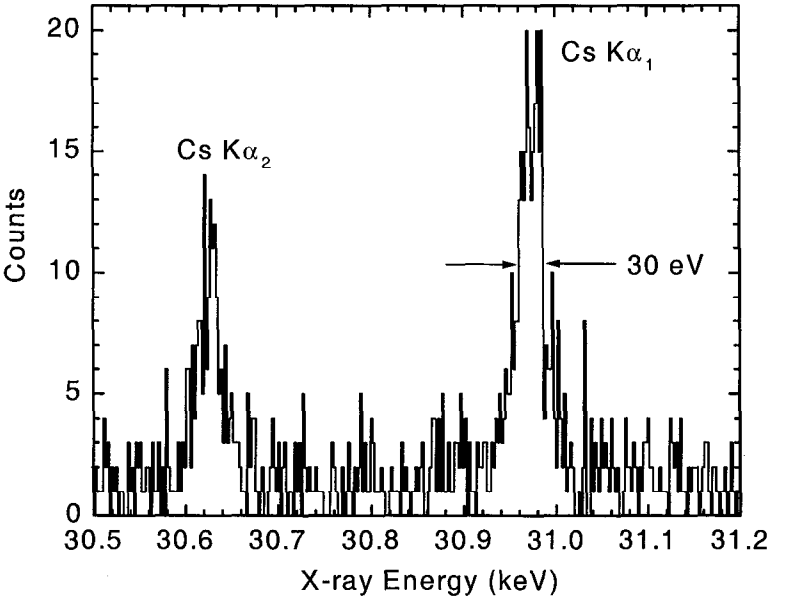

FIGURE 3. Highly resolved spectrum of the cesium $K\alpha$ radiation emitted by a ^{133}Ba radioisotope, demonstrating the feasibility of the transmission–type spectrometer designed for high–resolution hard x–ray measurements at SuperEBIT.

$K\alpha$ SPECTRA OF XE^{53+} AND XE^{52+}

A sketch of the experimental setup, i.e., the implementation of the transmission–type curved crystal spectrometer at SuperEBIT, is shown in Figure 4. Operation of the spectrometer in monochromator mode requires a normalization of the counts, i.e., the number of diffracted x rays recorded with the detector labeled *GeX*, measured at each crystal position. The normalization which seemed best suited for these measurements is based on the number of xenon $K\alpha$ x rays emitted from the trap region. This was accomplished with the germanium detector labeled *GeSE* in Figure 4. Due to the cylindrical symmetry of the electron beam, all access ports

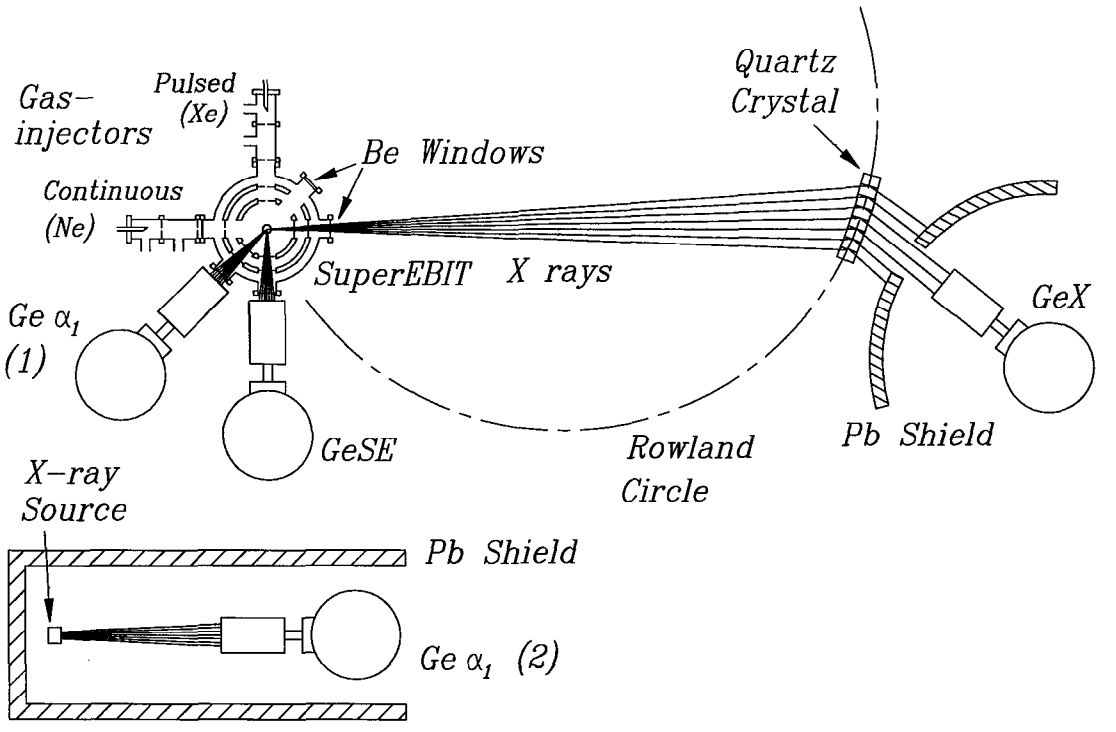

FIGURE 4. Sketch of the transmission–type curved crystal spectrometer setup. The electron beam, oriented perpendicular to the page, and the cylindrically bent crystal have to be part of the Rowland circle. The transmission spectrometer is operated in monochromator mode, i.e, a spectrum is obtained by rotating the crystal and recording the number of diffracted x rays with the germanium detector *GeX* as a function of the crystal position. Synchronized data acquisition between the germanium detectors *GeX* and *GeSE* is essential for the normalization of the measured high–resolution spectra. The energy of the Ly–α_1 transition was measured with the germanium detector, labeled *Ge* α_1. Xenon spectra *(1)* and calibration spectra *(2)* were taken successively in three–hour intervals.

receive the same type and amount of illumination over time, which makes a normalization by means of the measured flux at a different access port feasible. When the number of xenon Kα photons measured with this germanium detector (*GeSE*) reached a preset amount, the counting process for both detectors *GeX* and *GeSE* was stopped, the crystal moved into the next position, and the counting process restarted. The spectrum shown in Figure 5 is the result of several scans over the wavelength region of interest, i.e., over the various Xe^{52+} and Xe^{53+} $n = 2 \rightarrow 1$ lines.

The area of the germanium detector *GeX* that was used for recording the diffracted x rays was 1018 mm^2, about five times larger than the detector used for the measurement of the Cs Kα lines (Figure 3). Thus, the resolving power of the spectrometer for the highly charged xenon Kα measurement was somewhat smaller than for the Cs Kα measurement. In particular, $E/\Delta E \approx 900$ versus the

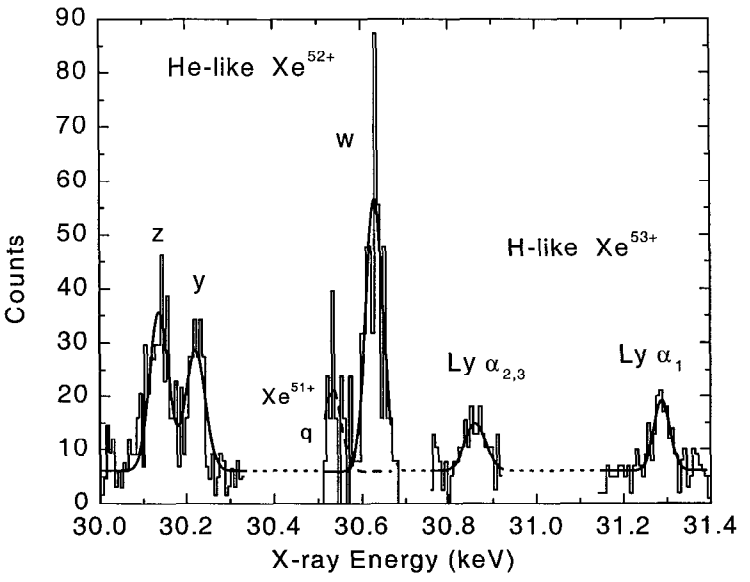

FIGURE 5. Spectrum of the Kα transitions of hydrogenlike Xe^{53+} and heliumlike Xe^{52+}. The spectrum shows the hydrogenlike $2p_{3/2} \rightarrow 1s_{1/2}$ (Ly–α_1) transition, and a blend of the $2p_{1/2} \rightarrow 1s_{1/2}$ and $2s_{1/2} \rightarrow 1s_{1/2}$ (Ly–$\alpha_{2,3}$) transitions, and the heliumlike $1s2p\,^1P_1 \rightarrow 1s^2\,^1S_0$ (w), $1s2p\,^3P_1 \rightarrow 1s^2\,^1S_0$ (y), and $1s2s\,^3S_1 \rightarrow 1s^2\,^1S_0$ (z) transitions. The dashed line indicates the lithiumlike $1s2s2p\,^2P_{3/2} \rightarrow 1s^2\,2s\,^2S_{1/2}$ (q) innershell transition. Each channel represents the number of detected photons accumulated over three steps, i.e., three consecutive crystal positions. The dispersion is about 6.6 eV per channel. A resolving power of 930 $\pm$ 110 was inferred from the fitted line widths. The total data acquisition time was 122 hours. The measured wavelengths were converted to energies using the wavelength–voltage product of 12398.4243 eV Å.

previously measured 1200. The use of a larger detector area was necessary because of the small x–ray flux emitted from the trapped xenon ions, e.g., the count rate for the Ly–α_1 line was only about 10 counts per hour. Overall, the xenon spectrum displayed in Figure 5 represents 122 hours of data acquisition time.

DETERMINATION OF THE ELECTRON–IMPACT EXCITATION CROSS SECTIONS

The electron–impact excitation cross sections are determined relative to the radiative recombination cross sections. The values used for the radiative recombination cross sections are theoretical predictions by Scofield [20]. These calculations are based on a relativistic Hartree Slater model which has proven to be in excellent agreement (within 3%) with measured cross section values of the inverse process, i.e., photoionization, for photon energies in the 10–keV to 100–keV range [25]. Unfortunately, the comparison between the calculated and measured values is only available for neutral elements, e.g., neutral xenon atoms. However, one can argue

that for the much simpler atomic structure of highly charged xenon ions, the accuracy of the calculated values should be at least comparable to the case of neutral xenon. In fact, measurements of the radiative electron capture of highly charged heavy ions have shown an agreement between theoretical and experimental cross section values of better than 5% [26,27].

Following steps are required for the determination of the electron–impact cross sections:

(i) Observation of the whole characteristic spectrum covering the transitions directly excited by electron impact and the radiative recombination lines. The resolution of the radiative recombination spectrum has to be sufficient for inferring the relative ion abundance.

(ii) High–resolution measurement of the direct excitation (DE) spectrum which shows the composition of the DE radiation with respect to the different ion species. Thus, the low–resolution spectrum of the DE lines (see previous step) can be divided into the various spectral features observed with the high–resolution instrument.

(iii) Conversion of the measured differential cross section values into total cross sections.

(iv) Extraction of the electron–impact excitation cross section by accounting for the various atomic processes in SuperEBIT that generate emission of the characteristic x rays.

The information obtained with the spectra displayed in Figures 1 and 5 address the points (i) and (ii) listed above. Since the high–resolution spectrum of the DE lines is taken with a crystal spectrometer, the measured line intensities have to be corrected with respect to the polarization of the line emission before the spectra are compared with the low–resolution germanium detector measurements. Because of the small Bragg angles encountered during the high–resolution measurement, i.e., from 9.67° to 10.04°, the adjustment of the line intensities due to polarization is less than 3% , much smaller than the uncertainties introduced by the low number of counts in each line. The information of the polarization of the recorded spectral lines is also important for step (iii), the conversion to total cross sections. The experimental setup is designed for measuring the radiation emitted perpendicular to the electron beam. The total cross sections are inferred using the relation between the overall amount of emitted radiation of a dipole source and the intensity in perpendicular direction with respect to the dipole axis accounting for the polarization of the radiation [28].

The last step, item (iv), requires an estimate of the magnitude of contributions which populate the $n = 2$ levels due to processes other than direct electron–ion impact excitation of a ground state electron. In SuperEBIT, the important atomic processes that populate the L–shell of trapped hydrogenlike and heliumlike ions are:

- Radiative recombination onto the n = 2 levels,
- Radiative recombination onto n > 2 levels, followed by cascades that include a $n' \rightarrow 2$ transition,
- Charge exchange processes between neutrals and highly charged xenon ions, followed by cascades that include a $n' \rightarrow 2$ transition,
- Inner–shell ionization of lithiumlike xenon ions,
- Electron–impact excitation from the ground state to n > 2 levels, followed by cascades that include a $n' \rightarrow 2$ transition, and
- Direct electron–impact excitation, i.e., from the ground state to n = 2.

A schematic diagram regarding these processes is shown in Figure 6. The impact

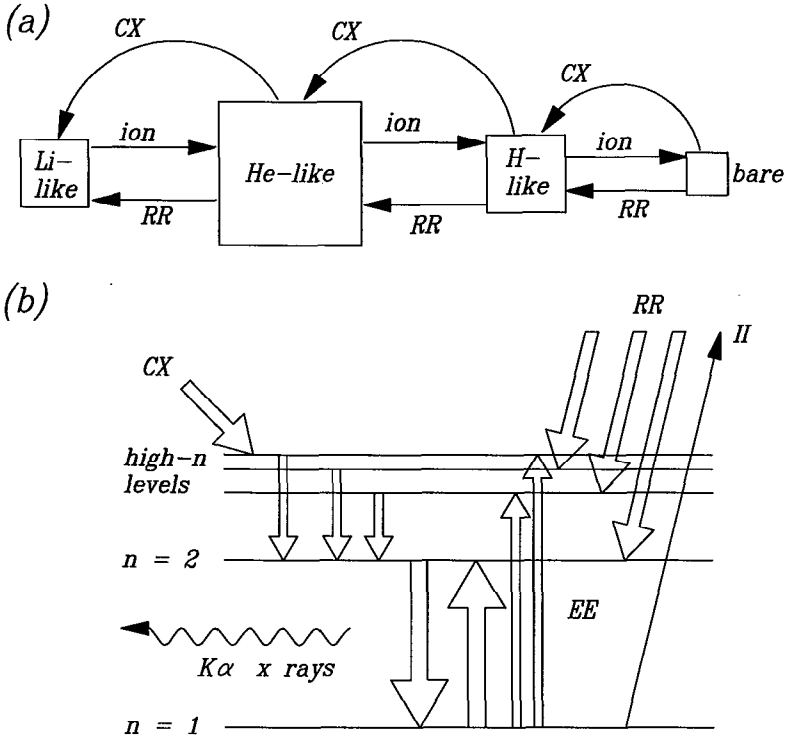

FIGURE 6. Schematic diagram of the main processes that effect **(a)** the charge balance and **(b)** the population of the n = 2 levels of the trapped highly charged ions. Included are charge exchange reactions between neutrals and ions (CX), radiative recombination (RR), and electron–impact ionization (ion). The area of each box is proportional to the abundance. The processes which populate the n = 2 levels and, thus, contribute to the measured intensity of the Kα radiation are sketched in **(b)**. II symbolizes the innershell ionization of lithiumlike xenon ions.

of the radiative recombination on the n = 2 level population was estimated using

theoretical values of the radiative recombination cross sections for electron capture onto n < 5 levels. The contribution due to charge exchange processes was determined using measurements of the K–shell x–ray emission of heliumlike and hydrogenlike xenon after electron capture due to charge exchange with neutrals. For these measurements, SuperEBIT was operated in the magnetic trapping mode [29,30]. The amount of enhanced Kα x–ray emission caused by inner–shell ionization of lithiumlike xenon has been estimated by applying electron–impact ionization cross sections derived from the Lotz formula [31,32]. The population of the L–shell in the hydrogenlike and heliumlike xenon due to electron–impact excitation of n > 2 levels followed by cascades that include a n′ → 2 transition and due to direct electron–impact excitation of n = 2 levels was estimated using radiative and collisional rate calculations for all n = 2, 3, and 4 levels based on the Hebrew University / Lawrence Livermore Atomic Code (HULLAC). Table 2 gives an overview of these estimates, i.e., of the contributions due to processes other than electron–impact excitation of the n = 1 → 2 transitions, in terms of electron–ion interaction cross–section equivalent values, denoted $\tilde{\sigma}$. The extracted electron–impact excitation cross–sections are also listed in Table 2.

TABLE 2. Electron impact excitation (EE) cross sections for the n = 1 → 2 transitions in heliumlike and hydrogenlike xenon. The values are extracted from the measured total cross sections after accounting for radiative recombination (RR), innershell ionization (II), and charge exchange (CX) reactions with neutrals. The contributions are given in the form of an electron–ion interaction equivalent cross section (notation $\tilde{\sigma}$), e.g., the cross section values representing the contribution due to CX are not the actual CX cross sections. The factor f_{pop} is the fraction of the n = 2 level population that is due to direct n = 1 → 2 electron–impact excitation. Thus, $1-f_{pop}$ describes the relative population of the n = 2 levels due to electron–impact excitation into n > 2 levels followed by cascades. The uncertainties listed combine statistical uncertainties and uncertainties in the contribution from the adjustments with respect to the RR, CX, and II processes. No systematic uncertainties due to the use of theoretical models have been added.

line	σ_{expt} barn	$\tilde{\sigma}_{RR}$ barn	$\tilde{\sigma}_{CX}$ barn	$\tilde{\sigma}_{II}$ barn	f_{pop}	σ_{EE} barn
Ly–α_1	9.8 ± 1.6	0.146 ± 0.013	0.57 ± 0.26	—	0.944	8.6 ± 1.5
Ly–$\alpha_{2,3}$	10.4 ± 3.7	0.734 ± 0.064	0.50 ± 0.23	—	0.904	8.2 ± 3.4
w	11.8 ± 1.8	0.127 ± 0.009	4.29 ± 0.99	—	0.950	7.0 ± 2.0
y	7.4 ± 1.4	0.332 ± 0.023	3.00 ± 0.63	—	0.953	3.9 ± 1.5
z	11.3 ± 1.8	0.388 ± 0.027	3.43 ± 0.72	2.71 ± 0.84	0.227	1.08 ± 0.48

The experimentally achieved electron–impact excitation cross sections are compared with three sets of theoretically predicted values. All three sets are based on a distorted–wave approach [33,34], two sets are relativistic calculations, and one of the two relativistic calculations also includes the Breit interaction between the free and the bound electrons [35,36]. The comparison is presented in Table 3 and in graphical form in Figure 9. The uncertainties of the measured cross sections only

TABLE 3. Comparison between the measured (σ_{EE}) and calculated electron–impact excitation cross sections. The calculated values are based on a distorted–wave approach [33,34]. Relativistic effects certainly play an important role in the interaction between the 112–keV beam electron and the highly charged xenon ion as seen in the large difference between the non–relativistic calculations, $\sigma_{non-rel}$, and the relativistic calculations, σ_{rel}. Additionally, the impact of the Breit interaction between the free and the bound electrons is significant in the excitation process of the heliumlike xenon. Thus, agreement between the measured and calculated cross section values can only be found when the Breit interaction, i.e., the Generalized Breit Interaction [35,36], is included in the calculations, σ_{GBI}.

line	σ_{EE} barn	$\sigma_{non-rel}$ barn	σ_{rel} barn	σ_{GBI} barn
Ly–α_1	8.6 ± 1.5		8.256	8.109
Ly–$\alpha_{2,3}$	8.2 ± 3.4		6.541	6.787
w	7.0 ± 2.0	21.64	17.45	8.364
y	3.9 ± 1.5	0.127	7.313	3.842
z	1.08 ± 0.48	0.123	0.172	0.152

reflect the uncertainties due to the low counts in the measured spectral lines. The systematic uncertainty introduced by tying the measured values to theoretical values of the radiative recombination cross sections, by using theoretical predictions for the polarization of the spectral line emission, and by applying the HULLAC code for estimating the population of the n = 2 levels due to cascades have not been included.

MEASUREMENT OF THE TRANSITION ENERGIES

The high precision of the crystal holder rotation mechanism allows a very accurate determination of the dispersion of the recorded high–resolution spectra. However, the transmission spectrometer in its current setup is not equipped for absolute Bragg angle measurements, and the determination of the wavelengths requires the observation of at least one calibration line. Therefore, the wavelengths were measured relative to the Ly–α_1 line, and a calibration of the Ly–α_1 transition energy was performed in a separate experiment. This Ly–α_1 transition energy measurement was performed parallel to the high–resolution transmission–type curved crystal spectrometer measurement discussed above. A state–of–the–art germanium detector[5] was used for successively observing the Kα x–ray radiation emitted by the highly charged xenon ions in the trap and the spectra of x–ray sources containing the Kα emission of cesium and barium. The detector is labeled *Ge* α_1 in the experimental setup which is shown in Figure 4. With a resolution of about

[5] High–purity germanium detector with a planar crystal geometry from EG&G ORTEC, Model No. GLP 16195/10.

270 eV at photon energies of about 31 keV, this detector is suitable for resolving the xenon Ly–α_1 transition, which is separated from the adjacent spectral features, the Ly–$\alpha_{2,3}$ blend and the $1s2p\,^1P_1 \rightarrow 1s^2\,^1S_0$ transition in heliumlike xenon by more than 400 eV.

In three hour intervals the detector was switched between the SuperEBIT observation port and a well shielded calibration stand (see Figure 4), where the detector dispersion was calibrated utilizing the Kα fluorescence of cesium and barium. In particular, the calibration stand was equipped with the radioisotope ^{133}Ba, which after K–shell electron capture emits the Cs Kα x–rays, and the radioisotope ^{241}Am, which was covered with a barium window, thus, producing the Ba Kα fluorescence. The calibration stand was adjusted in such a way that the count rate of the Cs Kα emission was about twice the average count rate of the Xe Ly–α_1 transition. Therefore, the count rate for the Cs Kα_1 x rays was higher, and for the Cs Kα_2 x rays was lower than the count rate for the Xe Ly–α_1 x rays. Matching the count rates for measurement and calibration is important for high–precision measurements, since the electrical field across the germanium crystal and, thus, the magnitude of the detected current pulse, is sensitive to the amount of electron–hole pairs created by photon impact. A spectrum combining the barium, cesium, and highly charged xenon Kα emission is presented in Figure 7.

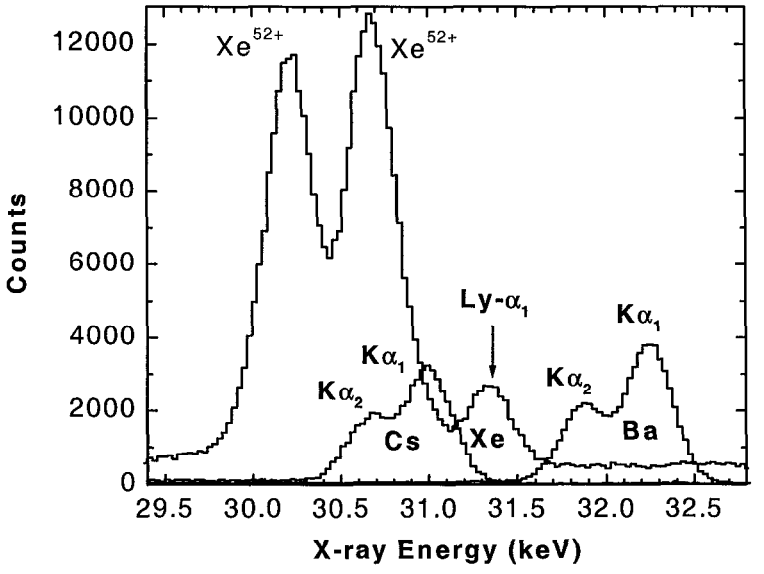

FIGURE 7. Kα spectra of highly charged xenon ions, cesium, and barium. The cesium fluorescence is emitted by a ^{133}Ba radioisotope, which after capturing a K–shell electron converts into an innershell excited ^{133}Cs*. The barium Kα radiation is emitted by a barium foil which is illuminated with the radioisotope ^{241}Am causing K–shell photoionization in the barium. All three spectra together represent about 12 hours of data acquisition time.

The centroid positions of the spectral features were determined using a line–shape function that accounts for the response of the germanium detector, i.e, Compton profile and escape–peak behavior. Figure 8 shows the line centroid values as a function of SuperEBIT runtime. This plot clearly emphasizes the importance of

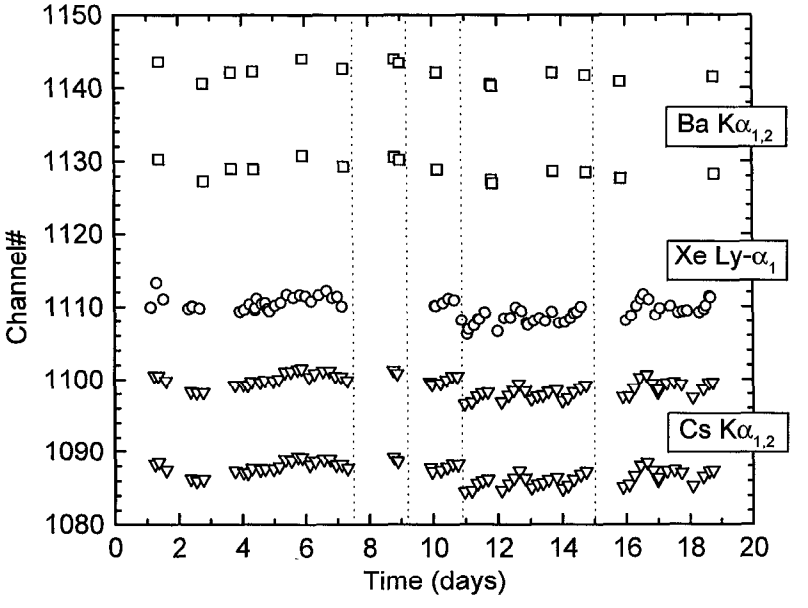

FIGURE 8. Centroid positions of the spectral lines given in the arbitrary quantity *Channel Number* recorded with a germanium detector as a function of the SuperEBIT runtime, i.e., the duration of the experiment. The statistical uncertainties for the centroid positions are smaller than the size of the symbols used in this plot. Thus, the shifts in the centroid positions are significant. The dashed lines indicate when the high voltage power supply for the detector was turned off.

continuous calibration. Otherwise, the long–term drift of the pulse–height signal of the detector introduces a systematic uncertainty which is more than an order of magnitude bigger than the statistical uncertainty based on the number of counts in the spectral line. The barium Kα fluorescence, for example, was only measured twice a day and, thus, the observed shift of the line centroid in time does not contain the details necessary for an accurate tracking of the shifts in the germanium detector's pulse–height signal.

The energy values for the calibration lines are taken from the *CRC Handbook for Chemistry and Physics* [37] and are listed in Table 4. These values are taken from a paper by Bearden published in 1967 [38] and require correction due to changes in the value for the voltage–wavelength product and the value for the conversion factor of the wavelength units, $V\lambda = 12398.4243$ eV Å ± 0.60 ppm, $Å^*/Å = 1.00001481 \pm 0.92$ ppm [39]. The Å*/Å correction incorporates also the most recent result of the 2d spacing of the (220) oriented lattice planes in a nearly perfect silicon crystal, $d_{220} = 1.92015540$ Å ± 0.21 ppm [40,41]. Additional adjust-

ment is required for the uncertainties, which reflect the probable error (abbreviated as "p.e." in the wavelength and energy compilation by Bearden) which is defined as a 50% confidence limit, and does not include the uncertainty of the Å* unit due to the uncertainty of the W Kα_1 measurement. Even though the original paper [38] emphasizes the fact that Gaussian statistics was not applicable for most data, it seems to be the standard approach to convert the "p.e." values to a 67% confidence limit by assuming Gaussian distribution and, thus, to multiply the uncertainty values by a factor of 1.48 (e.g. [42–44]). Table 4 also lists the most recent measurement available for the barium Kα transition energies [45] and the transition–energy values that are currently used by the Quantum Metrology Group at the National Institute of Standards and Technology (NIST) [46].

TABLE 4. Transition energies of the cesium and barium calibration lines. The energy values in column E_{67} are taken from the compilation published by Bearden [38]. These values are also listed in the *Handbook of Chemistry and Physics* [37]. $E_{67,adj}$ are the adjusted energy values incorporating the current values for the x–ray standards [39] and the most recent measurement of the Si (220) 2d spacing [40,41]. For the Kα emission of barium a more recently measured value is available, $E_{82,adj}$ [45]. This value, too, was adjusted to the current x–ray standards. Column E_{99} lists the transition energies currently used at NIST [46].

Line	E_{67} eV	$E_{67,adj}$ eV	$E_{82,adj}$ eV	E_{99} eV
Cs Kα_2	30625.1(3)	30626.32(44)		30625.42(45)
Cs Kα_1	30972.8(3)	30974.06(46)		30973.15(46)
Ba Kα_2	31817.1(4)	31818.39(61)	31816.62(6)	31816.631(60)
Ba Kα_1	32193.6(3)	32194.89(50)	32193.27(7)	32193.279(70)

The result of the Ly–α_1 transition energy measurement is given in Table 5 together with the theoretically predicted value from Johnson and Soff [47]. Surprisingly, there is a significant disagreement between the measured and the calculated values. The disagreement is much larger than the changes in the measured value due to using the different sets of calibration line values from Table 4. A suggested explanation for this unexpected disagreement is given in the section titled "Discussion".

TABLE 5. Measurement of the Xe^{53+} Ly–α_1 transition energy. The measured value E_1 was obtained utilizing the calibration set $E_{67,adj}$ from Table 4. Using $E_{82,adj}$ and E_{99} yields the values E_2 and E_3, respectively. The measured values are compared to the theoretical prediction by Johnson and Soff, labeled $E_{J\&S}$ [47].

E_1 eV	E_2 eV	E_3 eV	$E_{J\&S}$ eV
31279.2 ± 1.5	31278.8 ± 1.5	31278.1 ± 1.5	31283.77 ± 0.09

Using both the theoretical and the measured values for the xenon Ly–α_1 tran-

sition energy, the transition energies and wavelengths, respectively, for all spectral features observed in Figure 5 have been determined. For example, taking the theoretically predicted value [47], i.e., 31283.77(9) eV and 0.396321(1) Å, respectively, and a 2d–spacing of 2.3604 Å for the $(13\bar{4}0)$–oriented Quartz crystal yields a Bragg angle of 9.6660 °. The distance to the centroid of the neighboring Ly–$\alpha_{2,3}$ blend is 380.0 steps with the stepper motor that controls the crystal position. This crystal rotation is equivalent to a Bragg angle difference of 0.136° and, thus, the wavelength of the neighboring Ly–$\alpha_{2,3}$ blend is 0.40183 Å. The wavelengths values are converted to transition energies for easier comparison with theoretical predictions, and the result is presented in Table 6 and in graphical form in Figure 10. The accu-

TABLE 6. Comparison of the measured and calculated energies for the n = 2 → 1 transitions in hydrogenlike and heliumlike xenon. The first set of experimental results E_{expt} is calibrated by utilizing the measured value of the Ly–α_1 transition, i.e., 31279.2(27) eV. The E_{exth} values have been determined relative to the theoretical value for the Ly–α_1 line, i.e., 31283.77(9) eV [47]. The result of the hydrogenlike transitions is compared to the calculations by Johnson and Soff $E_{J\&S}$ [47]. For the heliumlike transitions the theoretical values are from Drake E_D [48], Plante, Johnson and Sapirstein E_P [49], and Chen, Cheng, Johnson and Sapirstein E_C [50,51].

Hydrogenlike transitions

Line	E_{expt} eV	E_{exth} eV	$E_{J\&S}$ eV
Ly–α_1	31279.2 ± 2.7	31283.8 ± 2.3	31283.77
Ly–α_2	30850.4 ± 5.7	30855.0 ± 5.7	30856.36
Ly–α_3			30863.49

Heliumlike transitions

Line	E_{expt} eV	E_{exth} eV	E_D eV	E_P eV	$E_{C\&C}$ eV
w	30619.9 ± 4.0	30624.5 ± 4.0	30629.28	30629.68	30630.64
x	—	—	30593.54	30593.93	30594.96
y	30210.5 ± 4.5	30215.1 ± 4.5	30205.58	30205.87	30206.90
z	30126.7 ± 3.9	30131.3 ± 3.9	30128.40	30128.78	30129.79

racy is currently limited by counting statistics. In fact, an increase in the number of counts of at least a factor of 10 would be necessary to match the much lower uncertainty associated with the determination of the dispersion of the transmission–type curved crystal spectrometer.

DISCUSSION

Electron–impact excitation cross section measurement

The result of the electron–impact excitation cross section measurement is summarized in Figure 9. The comparison between the measured and the theoretically predicted cross sections shows that relativistic effects, in particular, the Breit interaction between the free and the bound electrons, are significant. Especially, for the

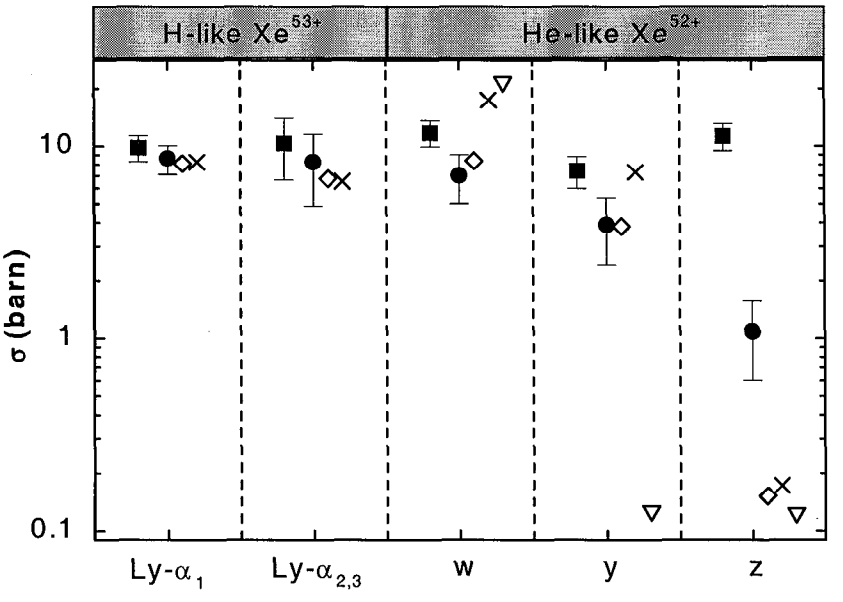

FIGURE 9. Comparison between the experimental and theoretical values for the electron impact excitation cross section of the n = 1 → 2 transitions in heliumlike and hydrogenlike xenon. The plot shows two sets of measured total cross section values. The first set (filled squares) represents the "overall" cross sections without accounting for the various processes that populate the L–shell of the xenon ions. The second set (filled circles) represents the extracted electron–impact excitation cross sections. The calculated values are based on a distorted–wave approach [33,34]. Neglecting relativistic effects yields the ▽ values. The symbol × denote relativistic calculations but without accounting for the Breit interaction between the free and the bound electrons. Incusion of the Breit interaction yields the values marked by the ◇ symbol [35,36]. The uncertainties shown are statistical uncertainties only.

excitation of the heliumlike Xe^{52+} ground states by impact of 112–keV electrons, agreement between the theoretical and experimental values can only be found when the Breit interaction is included in the calculations, even though the uncertaintics of the measured values are in the 20% to 50% range. Moreover, no agreement exists for the excitation cross section of the $1s^2\,{}^1S_0 \rightarrow 1s2s\,{}^3S_1$ transition (line z). The disagreement in case of line z reflects most likely the complexity of the population mechanism of this metastable level in the heliumlike ion. For the hydrogenlike lines

we found good agreement for both calculations, with and without inclusion of the Breit interaction. Besides the differences in the calculated values depending on the inclusion of various effects, Figure 9 also shows the impact on the population of the L–shell of the xenon ions due to effects other than direct electron–impact excitation from the ground state — visualized by the difference between the two sets of experimental values. In other words, the two sets of measured cross section values in Figure 9 indicate the fraction of the n = 2 → 1 x–ray emission which is caused by direct n = 1 → 2 electron–impact excitation. While the emission in hydrogenlike Xe^{53+} is clearly dominated (more than 80%) by direct excitation, less than 60% of the emission in heliumlike Xe^{52+} is due to direct excitation of the ground state. In fact, for line z, direct excitation only accounts for about 10% of the observed emission, making the cross section value for line z strongly dependent on the models utilized for simulating the population mechanism.

Determination of the n = 2 → 1 transition energies

The predictions for the transition energies in hydrogenlike systems have shown agreement with most experimentally obtained values and, thus, the theoretical values are widely accepted as being accurate, e.g. [2]. Therefore, it is common practice to use spectral lines of hydrogenlike ions to calibrate the dispersion of the spectroscopic instrumentation, e.g. [52]. In fact, a calibration with lines emitted by hydrogenlike ions is more precise than utilizing the Kα emission of neutral elements because the hydrogenlike lines are not affected by unresolved satellites due to shake processes. Additionally, the natural line width is much smaller for lines emitted by hydrogenlike ions than by inner–shell excited neutrals. Nevertheless, the characteristic emission of hydrogenlike ions has not been accepted as an x–ray standard, yet. Therefore, a calibration with respect to the current x–ray standard, i.e., the tungsten Kα_1 line, and to secondary standards, respectively, was performed. Surprisingly, the calibration measurement yielded a value for the Ly–α_1 transition energy that disagreed with the theoretical value significantly. For the wavelength calibration of the observed n = 2 → 1 transitions, both the theoretical and the measured values for the Ly–α_1 line were used. Thus, the comparison between theory and experiment shown in Figure 10 contains two sets of experimental data.

The 4.6–eV difference between the measured and calculated transition energy of the Ly–α_1 line (see Table 5) is equivalent to a deviation of more than 3 σ[6]. However, since the calculations for the transition energies of the hydrogenlike isoelectronic sequence have proven to be successful in so many comparisons with measurements, it is very likely that this significant disagreement is due to a shortcoming in the experimentally obtained result.

One suggestion for the disagreement is a systematic uncertainty introduced by the calibration line values. A weakness of the wavelengths reference table compiled

[6] The probability of finding a data point outside the 3–σ confidence limit is less than 0.3%.

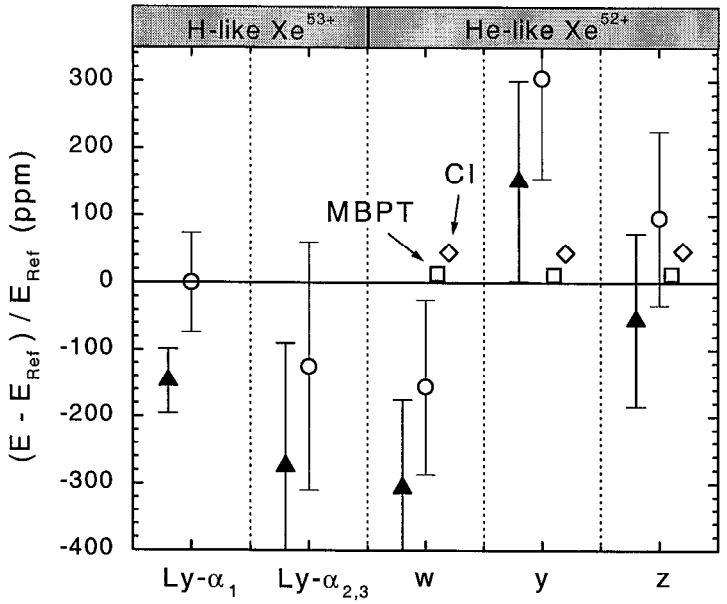

FIGURE 10. Relative deviation between measured and theoretically predicted transition energies for the hydrogenlike and heliumlike xenon Kα lines. The transition energies have been measured relative to the xenon Ly-α_1 line. The filled-triangle data set utilizes the measured value of the Ly-α_1 transition energy, i.e., 31279.2(27) eV, the data set marked by the open circles is obtained using the value calculated by Johnson and Soff, i.e., 31283.77(9) (see Table 5). The reference energies (E_{Ref}) for the hydrogenlike lines are from Johnson and Soff [47]. For the heliumlike transition energies the values calculated by Drake using the unified method are taken as a reference [48]. The □ values were calculated by Plante et al. [49] summing all-orders of many-body perturbation theory (MBPT). The ◇'s represent the values obtained by Cheng et al. and Chen et al. [50,51] applying relativistic configuration interaction (CI) calculations combined with *ab initio* QED calculations.

by Bearden [38] is the assignment of the wavelengths to the peak of the observed spectral feature. For a symmetric line profile the peak value is identical with the centroid, thus, the given value is inert with respect to applications involving spectrometers of different resolving power. For asymmetric spectral features, however, the peak value can only be reproduced utilizing the same type of spectrometer used for measuring the tabulated wavelength values. Otherwise, the peak value might not reflect the same position on the wavelength scale due to the different response function of the spectrometers. Recent high-resolution measurements of K-shell and L-shell emission of neutrals after electron impact have shown a significant contribution of satellite lines, causing an asymmetry of the observed spectral profile [53-55]. The presence of all these satellites also shows the internal complexity of the inner-shell processes, especially in high-Z elements. In contrast to the electron-impact based x-ray sources, the emission of the radioisotopes used for the calibration are much less affected by M-satellite structure. Unfortunately,

the counting statistics in the spectrum shown in Figure 3 is not sufficient for a conclusive analysis regarding the contribution to the measured line emission due to satellites. In conclusion, the disagreement between the measured and the calculated transition energy of the xenon Ly–α_1 line emphasizes the need for a re–evaluation of the commonly used x–ray wavelengths table for atomic inner–shell transitions, in particular, for the cesium Kα lines.

ACKNOWLEDGMENTS

We thank Ed Magee and Dan Nelson for technical support and Honglin Zhang for providing us with the theoretical cross section values that include the Breit interaction. This work was performed under the auspices of U.S.DOE by Lawrence Livermore National Laboratory under Contract No. W–7405–ENG–48.

REFERENCES

1. H. Persson *et al.*, Hyperfine Inter. **108**, 3 (1997).
2. H. F. Beyer, H.-J. Kluge, and V. P. Shevelko, in *X–Ray Radiation of Highly Charged Ions, Atoms and Plasmas* (Springer, Heidelberg, 1997), Chap. 3 "Atomic Structure and Spectra", pp. 61–84, comparison of Lamb–shift measurements in Table 3.16, pg. 82.
3. J. Schweppe *et al.*, Phys. Rev. Lett. **66**, 1434 (1991).
4. P. Beiersdorfer *et al.*, Phys. Rev. Lett. **71**, 3939 (1993).
5. P. Beiersdorfer *et al.*, Phys. Rev. A **52**, 2693 (1995).
6. P. Beiersdorfer *et al.*, Phys. Rev. Lett. **80**, 3022 (1998).
7. T. Beier, G. Plunien, and G. Soff, Hyperfine Inter. **108**, 19 (1997).
8. S. Chantrenne, P. Beiersdorfer, R. Cauble, and M. Schneider, Phys. Rev. Lett. **69**, 265 (1992).
9. K. Wong, P. Beiersdorfer, K. Reed, and D. Vogel, Phys. Rev. A **51**, 1214 (1995).
10. L. Horton, Phys. Scr. **T65**, 175 (1996).
11. J. Briand *et al.*, Z. Phys. A **318**, 1 (1984).
12. P. Indelicato, J. Briand, M. Tavernier, and D. Liesen, Z. Phys. D **2**, 249 (1986).
13. K. Widmann, P. Beiersdorfer, V. Decaux, and M. Bitter, Phys. Rev. A **53**, 2200 (1996).
14. M. Levine, R. Marrs, D. Knapp, and M. Schneider, Phys. Scr. **T22**, 157 (1988).
15. M. Levine *et al.*, in *International Symposium on Electron Beam Ion Sources and Their Applications, AIP Conference Proceedings No. 188*, edited by A. Hershcovitch (AIP Press, Woodbury, New York, 1989), pp. 82–101.
16. D. Knapp *et al.*, Nucl. Instr. and Meth. in Phys. Res. A **334**, 305 (1993).
17. S. Utter, P. Beiersdorfer, J. Crespo López-Urrutia, and K. Widmann, Nucl. Instr. and Meth. in Phys. Res. A **428**, 276 (1999).
18. M. B. Schneider *et al.*, in *International Symposium on Electron Beam Ion Sources and Their Applications, AIP Conference Proceedings No. 188*, edited by A. Hershcovitch (AIP Press, Woodbury, New York, 1989), pp. 158–165.

19. B. Penetrante *et al.*, Phys. Rev. A **43**, 4873 (1991).
20. J. H. Scofield, Phys. Rev. A **40**, 3054 (1989).
21. D. Vogel, P. Beiersdorfer, V. Decaux, and K. Widmann, Rev. Sci. Instrum. **66**, 776 (1995).
22. J. W. DuMond, Rev. Sci. Instrum. **18**, 626 (1947).
23. J. Kirz *et al.*, X–ray data booklet, Center for X–ray Optics, Lawrence Berkeley National Laboratory, University of California, Berkeley, California 94720 (1986).
24. G. Zschornack, *Atomdaten für die Röntgenspektralanalyse* (Springer-Verlag, Berlin, 1989).
25. E. Saloman, J. Hubell, and J. Scofield, At. Data Nucl. Data Tables **38**, 1 (1988).
26. T. Stöhlker, P. Mokler, C. Kozhuharov, and A. Warczak, Comments on Atomic and Molecular Phys. **33**, 271 (1997).
27. T. Stöhlker *et al.*, Phys. Rev. Lett. **82**, 3232 (1999).
28. I. Percival and M. Seaton, Phil. Trans. Royal Soc. London **251**, 113 (1958).
29. P. Beiersdorfer, L. Schweikhard, J. Crespo López-Urrutia, and K. Widmann, Rev. Sci. Instrum. **67**, 3818 (1996).
30. P. Beiersdorfer *et al.*, Phys. Scr. **T80**, 121 (1999).
31. W. Lotz, Astrophys. J. **XVI**, 207 (1967), supplement Series.
32. W. Lotz, Z. Phys. **216**, 241 (1968).
33. H. Zhang, D. Sampson, and R. Clark, Phys. Rev. A **41**, 198 (1990).
34. H. Zhang and D. Sampson, Phys. Rev. A **47**, 208 (1993).
35. C. J. Fontes, D. H. Sampson, and H. L. Zhang, Phys. Rev. A **47**, 1009 (1993).
36. C. J. Fontes, H. L. Zhang, and D. H. Sampson, Phys. Rev. A **59**, 295 (1999).
37. D. R. Lide and H. Frederikse, in *CRC Handbook of Chemistry and Physics*, 70 ed. (CRC Press Inc., Boca Raton, FL, 1989-1990), Chap. "X–ray Wavelengths", pp. E152–E190.
38. J. Bearden, Rev. Mod. Phys. **39**, 78 (1967).
39. E. R. Cohen and B. N. Taylor, Rev. Mod. Phys. **59**, 1121 (1987).
40. E. Kessler Jr. *et al.*, J. Res. Nat. Inst. Stand. Technol. **99**, 1 (1994), pp. 1–18 article; p. 285 Errata to this article.
41. P. Becker *et al.*, PTB-Mitteilungen **105**, 95 (1995).
42. E. Kessler Jr., R. Deslattes, A. Henins, and W. Sauder, Phys. Rev. Lett. **40**, 171 (1978).
43. E. Kessler Jr., R. Deslattes, and A. Henins, Phys. Rev. A **19**, 215 (1979).
44. T. Mooney *et al.*, Phys. Rev. A **45**, 1531 (1992).
45. E. Kessler Jr. *et al.*, Phys. Rev. A **26**, 2696 (1982).
46. Dr. Richard D. Deslattes, Quantum Metrology Group, NIST, Gaithersburg, MD 20899, private communication.
47. W. Johnson and G. Soff, At. Data Nucl. Data Tables **33**, 405 (1985).
48. G. Drake, Can. J. Phys. **66**, 586 (1988).
49. D. Plante, W. Johnson, and J. Sapirstein, Phys. Rev. A **49**, 3519 (1994).
50. M. Chen, K. Cheng, and W. Johnson, Phys. Rev. A **47**, 3692 (1993).
51. K. Cheng, M. Chen, W. Johnson, and J. Sapirstein, Phys. Rev. A **50**, 247 (1994).
52. P. Beiersdorfer, A. Osterheld, and S. Elliott, Phys. Rev. A **58**, 1944 (1998).
53. T. Ludziejewski *et al.*, Phys. Rev. A **54**, 232 (1996).

54. J.-C. Dousse and J. Hoszowska, Phys. Rev. A **56**, 4517 (1997).
55. J.-C. Dousse, J. Hoszowska, and O. Mauron, *Poster presentation*, 18th International Conference on X-ray and Inner-Shell Processes, Chicago, 23-27 August, 1999.